On broadening techniques for a high-resolution optical accelerometers

A. Amorosi [1,2], L. Amez-Droz [1,3], M. Zeoli [1,4], B. Thibaut [1], M. Teloi [2], M.H. Lakkis [1,2], A. Sider [1], C. Di Fronzo [1,2], C. Collette [1,3]
[1] Université de Liège, A&M Dept.,
Allée de la Découverte 9, B52/ Quartier Polytec 1, B-4000, Liège, Belgium
email: **anthony.amorosi@uliege.be**
[2] Université Libre de Bruxelles, BEAMS Dept. CP 165/56
Av. Franklin Roosevelt 50, B-1000, Bruxelles
[3] Université Libre de Bruxelles, TIPs Dept. CP 165/67
Av. Franklin Roosevelt 50, B-1000, Bruxelles
[4] Université Catholique de Louvain-la-Neuve, IRMP,
Chemin du Cyclotron 2, L7.01.05, B-1348 Louvain-la-Neuve, Belgium

Abstract

The paper discusses techniques for broadening the frequency bandwidth of a low natural frequency optical accelerometer to the [0.01 - 100] Hz band while preserving high resolution. The sensor mechanics is made of a leaf-spring suspended proof mass with a natural frequency of 2.8 Hz. The motion of the proof mass is read out with a custom design of a homodyne quadrature Michelson interferometer. The quadrature interferometer allows for precise measurement of the mass motion over several multiples of the laser wavelength (1550 nm) with a relative resolution measured at 2×10^{-13} m/$\sqrt{\text{Hz}}$ at 10 Hz. Two different strategies are employed for extending the corner frequency of the sensor bandwidth above the sensor mechanical frequency. They consist of a force feedback loop and an electronic filtering of the sensor's response. Both methods were experimentally applied and compared in terms of resolution. The sensor has a $10 \times 10 \times 10$ cm^3 compact design. The combination of the high-resolution readout and the large measurement bandwidth makes this sensor suitable for applications where high performance in the low-frequency regime is needed, namely active seismic isolation for ground-based scientific instruments (e.g. gravitational wave detectors) and ground compensation scheme in absolute quantum gravimeters.

I Introduction

Large-scale, ground-based, scientific instruments most often call for high-performance vibration isolation systems. Notorious examples are large telescopes [1], particle accelerators [2], high precision equipment such as lithography machines or atomic force microscopes [3], gravitational wave detectors [4–6], or gravimeters [7–10]. All these instruments make use of ground isolation systems consisting of passive elements (mechanical (anti-)springs, (inverted-)pendulums and dampers), active elements (utilising vibration sensors and actuators), or combinations of both. As the instruments get larger and the requirements on performance more stringent, the emphasis on high isolation levels in the low-frequency regimes (below 100 Hz) is becoming increasingly larger. This inevitably calls for active isolation systems with cutting-edge performance [11]. Active isolation systems utilise sensors to measure external disturbances or the motion of the payload requiring isolation. This signal is then fed to actuators to generate a counteracting force to stabilise the payload. The vibration sensors play a key role in the performance of the isolation system since one cannot isolate better than the motion the sensor can resolve. Similarly, the frequency bandwidth of the sensor is also critical since it directly relates to the frequencies that can be effectively isolated. This paper presents a design of an inertial accelerometer with high resolution (sub-nm/s^2) and broadband frequency response ([10 mHz - 100 Hz]) for use in active inertial isolation or vibration compensation schemes.

Inertial sensors based on interferometric readouts currently achieve better performance than conventional seismometers. Indeed, relative motion devices based on Michelson interferometry allow reaching resolutions that are up to 3 orders of magnitude better than electromagnetic devices traditionally used in seismometers [12–14]. These are currently standing at the state-of-the-art of relative motion sensing and only compete with a handful of technologies, usually also based on optical interferometry, such as Deep-Frequency Modulation (DFM) devices [15], Digitally Enhanced Interferometry (DEI) [16] or heterodyne interferometry [17] only to name a few. Using Michelson interferometers for reading out the proof-mass motion of inertial sensors therefore allows to push sensitivities of inertial sensors below the picometre level [18–25]. Other optical readout technologies (heterodyne interferometry, Fabry-Perot interferometry, DFM, etc) coupled to an inertial mass also commonly break through the picometre resolution [26–28]. The mechanical resonance frequency of the sensor also plays a role in the sensor sensitivity, as the resolution degrades as $1/\omega_0^2$ [29]. A high-resolution sensor therefore necessarily comes with low resonance frequency. Techniques exist for extending the bandwidth of sensors with a low mechanical resonance frequency to higher frequencies. One such method is the force-balance principle [30–32], which consists in feeding the reading of the sensor to an actuator to balance the proof-mass motion. This method is commonly used in broadband seismometers and has been shown to effectively extend the bandwidth while keeping the detectivity unchanged, under the assumption of negligible control noise. In addition, this method also improves the linearity of the sensor since the actuation reduces the proof mass motion and shifts the linearity requirements from the readout device to the actuator device. This is particularly valuable for accelerometers that use optical readout since fringe-counting interferometers suffer from strong non-linear behaviour [33]. Another method consists of using a frequency compensation filter for stretching the response of the sensor [29]. The method is widely used in analogue electronics and microelectronics [34], this paper suggests applying a similar operation for extending the accelerometer frequency response towards higher frequencies. This fundamentally consists of applying filtering to the sensor output which inverts the sensor frequency response and shapes it to the desired bandwidth. This method does not degrade the signal-to-noise ratio since it affects signal and noise equally. It also has the advantage of avoiding control and actuation noise that could be injected with the force-balance method. However, it does not reduce the sensor's non-linear behaviour.

The accelerometer presented in this paper builds upon the design of inertial sensors using an interferometric optical readout [25, 35–38]. The optical readout is a long-range quadrature Michelson interferometer whose fringes are demodulated in real time [39]. The sensor mechanics consists of a leaf-spring suspended pendulum, mimicking a LaCoste suspension with a more robust implementation [40, 41], designed with a 2.8 Hz natural frequency. Two different methods are employed to extend the bandwidth of the sensor by 2 orders of magnitude above its mechanical frequency. The first method is the force-balance principle. The force balance action is applied through a voice-coil actuator mounted on the proof mass. The actuator is equipped with a custom design of a quadrupole magnet consisting of 2 magnets with counter-facing polarisation [42–45]. This design causes the magnetic field of the assembly to decay much faster in the far field, decreasing Eddy-current damping and providing shielding against stray magnetic fields. The second method is the stretching of the sensor response using a frequency compensation scheme [29, 34]. The accelerometer is designed to be modular and can operate in either mode so both methods have been tested and compared. The sensor design fits a $10 \times 10 \times 10$ cm^3 box.

The paper first briefly presents the mechanical design of the optical accelerometer in section II. The homodyne quadrature Michelson interferometric readout is next presented in section III, where an experimental demonstration of the noise level is also shown. The two broadening approaches are then described in section IV where experimental noise floor and sensitivity bandwidth are shown. A qualitative and quantitative comparison is drawn in section V.

II Sensor assembly

The optical accelerometer is a 1D sensor sensitive to vertical acceleration. Figure. 1 shows a schematic of the sensor assembly and a picture of the prototype. The mechanics consist of a pendulum oscillating in a vertical frame, whose tip acts as the proof mass. The pendulum inertia is dictated by the inertial mass weighting 0.4 kg, and its centre of mass being located at 35 mm from the joint. The horizontal alignment of the pendulum

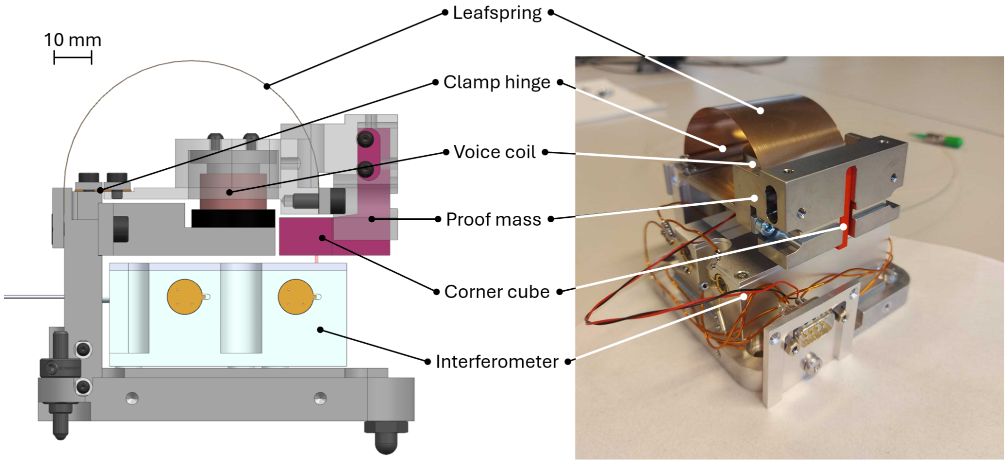

Figure 1: Side view of the optical sensor CAO (left) and actual assembly (right). The main assembly components are highlighted. The proof mass is a pendulum oscillating in a vertical frame. It is suspended horizontally with a leaf-spring blade ($CuBe_2$) and connected to the frame with a clamp hinge joint. The interferometer is mounted underneath the pendulum and targets a corner cube attached at its tip. A voice coil actuator is mounted below the pendulum. It is levelled with the hinge joint and placed at a location close to the proof mass centre of inertia.

is achieved using a copper-beryllium ($CuBe_2$) leaf-spring suspension blade. Such suspensions have been shown to be equivalent to a LaCoste pendulum and capable of achieving very long natural periods in a compact design [40, 41], while being more robust and practical to install than an actual LaCoste suspension. Copper-beryllium is chosen for its large elastic deformation range, which is required for withstanding the preloading of the blade. This suspension achieves a 2.8 Hz natural frequency and a 200 Q-factor. Since the targeted bandwidth for the accelerometer is [10 mHz - 100 Hz], a resonance frequency of around a Hz for the suspension was found to be a convenient trade-off between high resolution (low mechanical frequency) and large bandwidth (high mechanical frequency). The pendulum is connected to the body of the sensor through a clamped blade hinge joint, also in $CuBe_2$. The voice-coil actuator used for the feedback action is mounted below the pendulum structure. It is located below the proof mass centre of mass for the largest motion output to actuation effort ratio. It is also levelled with the clamped blade hinge joint. The voice coil is mounted in a moving magnet configuration, keeping the coil fixed to the frame to prevent damping caused by wire rubbing. The optical device is mounted below the pendulum on a tip-tilt stage used for the alignment of the interferometer. The interferometer targets a retroreflector mounted on the pendulum. The full sensor assembly fits in a 10 x 10 x 10 cm^3 volume. A detailed analysis of the sensor mechanics can be found in [46].

III Interferometric readout

Optical displacement readouts based on quadrature, long-range, Michelson interferometry currently allow reaching some of the highest state-of-the-art sensitivity and are therefore well suited for measuring small motions [12–14, 23, 38]. These readouts have demonstrated sub-picometre resolution when used as sensing elements in inertial devices [22,25,35]. The optical scheme of the interferometer used in this sensor is shown in Figure. 2 and is known as a homodyne, quadrature, Michelson interferometer [13]. The working principle is similar to that of a classical Michelson interferometer: the motion of the proof mass is read from the phase of the interferometer, as the two arms recombine at the beam splitter, where part of the beam is directed at a fixed reference mirror and the other is pointed to a corner-cube attached on the proof mass. The optical scheme features polarising elements and photodiodes, which causes two laser beams in phase quadrature to co-propagate in the interferometer. This then allows the measuring range to be extended over multiple wavelengths, whereas the range of a standard Michelson interferometer would be limited to motion up to a quarter of the laser wavelength only. Another main advantage of this optical scheme is the use of three

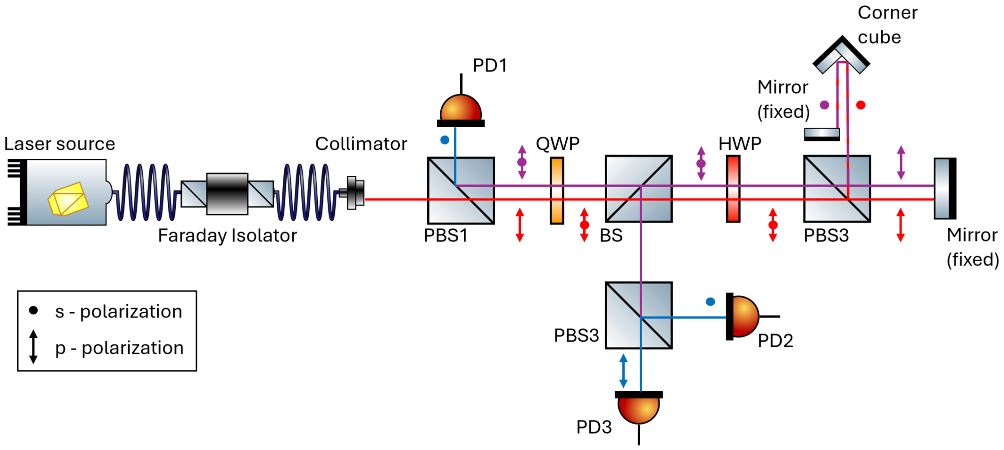

Figure 2: Quadrature interferometer optical scheme. The optical path towards the retro-reflecting mirrors and corner cube is shown in red, while the reflected path is shown in purple. The light intensities detected by the photodiodes are shown in blue. The polarisation state of the laser beam is indicated by arrows (p-polarisation) or a dot (s-polarisation). The two optical paths are shown off-axis for the sake of the clarity of the figure [25].

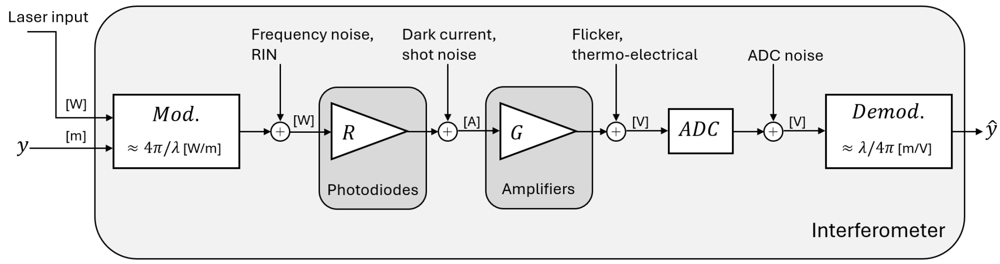

Figure 3: Quadrature interferometer noise diagram. The physical relative motion y is modulated in the phase of the interferometer. The displacement estimator $\hat{y}$ is reconstructed by demodulation of the interferometer signal. This estimator is entailed by the ADC quantisation noise, the electronics flicker and thermoelectrical noises, the photodiodes shot noise and dark current and the laser phase and RIN. R represents the photodiodes responsivity in [A/W] and G the TIA gains in [V/A].

photodiodes which allows to subtract common-mode noises on the photodiode. In particular, it makes the interferometer immune to laser intensity noise (RIN). This design however comes with a strong nonlinearity in the displacement reading for a large motion of the arms. A normalisation and ellipse correction algorithm is implemented before demodulating the interferometer phase. These allow the common-mode noise rejection and a linearisation of the reading. The working principle of these algorithms and the demodulation technique are extensively discussed in [13, 18, 36]. The algorithms have been implemented in real time for compatibility with applications in active isolation and ground compensation schemes [39]. An additional feature of the scheme is the ‘double-reflection’ strategy, which involves adding a second fixed mirror facing the moving corner cube. Indeed, despite the use of the corner cube to accommodate for the angular motion of the pendulum, large excursions of the proof mass still cause the beam reflected from the corner cube to undergo translational motion away from its incoming axis. This in turn causes the interference fringes to lose contrast and visibility, which translates into additional noise on the displacement reading and an enhanced non-linear behaviour. The addition of another flat mirror, fixed to the frame, sends the reflected beam toward the corner cube back on the axis of the incoming beam. This feature makes the interferometer assembly robust to large excursions of the proof mass, preserves an optimal interferometric contrast and eases the alignment process.

The readout noise is set by the quadrature sum of the interferometer’s internal noises. These are essentially: optical noises (photodiodes shot-noise and dark current), laser noise (RIN and phase/frequency noise) and electrical noises (resistors thermoelectrical noise, flicker noise and ADC quantisation noise). Descriptions

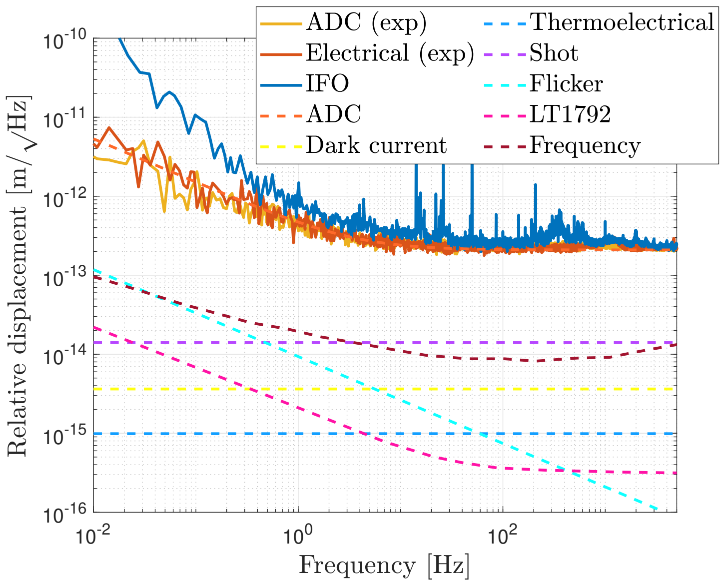

Figure 4: Resolution of the interferometric readout (IFO). The resolution is measured by mechanically blocking both arms of the interferometer to the same arm-length and recording the null signal. The measurement traces are shown in plain lines while theoretical models are shown in dashed lines. The sensor resolution matches the theoretical estimate and reaches 0.2 pm/$\sqrt{\text{Hz}}$ at high frequencies. The deviation of the experimental noise floor from the theoretical estimate at frequencies below 0.5 Hz is assumed to originate from temperature effects.

and models of these noise sources can be found in [13,29,47–49]. Figure. 3 shows how this noise propagates to the interferometer output. Note that the demodulation constant is given as an indication since the exact value is weighted by the interferometer contrast (quality of the alignment) and is precisely calculated during an initial characterisation process. The electrical and optical components of the interferometer were specifically chosen for their high resolution and low-noise performance. The laser source is a Koheras Adjustik X15 Distributed Feedback (DFB) fibre laser. It outputs a single-frequency, 1550 nm wavelength, laser beam with a sub-μrad/$\sqrt{\text{Hz}}$ phase noise at frequencies higher than 10 Hz. The laser beam is fed to the interferometer via an FC/APC polarisation maintaining optical fibre with an optical power of 4mW. The photodiodes are Thorlabs FGA21 InGaAs photodiodes, characterised by a responsivity $R = 1.04$ A/W and a Noise Equivalent Power (NEP) of 6×10^{-14} W/$\sqrt{\text{Hz}}$ at the nominal wavelength. They are operated in a photoconductive mode, under a bias voltage of 2.5 V, resulting in a typical dark current of 50 nA. The photocurrent is processed by a custom trans-impedance amplifier with a gain $G = 10000$ V/A using LT1792 low noise, precision, JFET input op-amp. The electrical components of this amplifier, especially resistors, were chosen to have Noise Indexes less than -30 dB to reduce the $1/f$ Flicker noise [50]. The output voltage is then recorded by a 16-bit, real-time, Microlab Box Analogue-to-digital converter. The interferometer resolution is measured from a blocked-mass test experiment where both arms of the interferometer are mechanically blocked at equal arm length. The null output signal, therefore, corresponds to the above-mentioned noise sources. The measured interferometer self-noise is shown in Figure. 4. It shows a noise floor 2×10^{-13} m/$\sqrt{\text{Hz}}$, dictated by the ADC noise. This matches with the theoretical estimate and noise-floor measurement of the acquisition system obtained by recording the output signal at different stages of the electronic chain when the input channels are shorted with an impedance matching the photodiodes impedance. At lower frequencies (< 1 Hz), however, the noise floor deviates slightly from the theoretical prediction and is currently assumed to originate from external effects such as temperature noise or optical fibre noise.

IV Broadening of the sensor response

IV.i Force-balance actuation

In force-feedback configuration, the sensor operates in closed loop according to the Force Balance Principle. Feeding back the motion of the proof-mass read by the interferometer to a force actuator allows to freeze the motion of the mass, improving the linearity of the sensor and extending its dynamic range and bandwidth without impacting the signal-to-noise ratio [30–32], if control noise can be assumed negligible. A contactless voice-coil actuator is used for the force-feedback because it can act on the proof mass of the sensor without impacting its dynamic. However, the permanent magnet of the voice-coil has experimentally been reported to generate Eddy currents in the surrounding conductive parts of the mechanics [42]. This velocity-dependent damping directly translates into thermal noise according to the Fluctuation-Dissipation theorem [51]. A careful design of the magnet allows to significantly reduce Eddy-current generation and its associated thermal noise by placing 2 magnets of identical strength in a quadrupole configuration, with like-poles facing each other [42–45]. With that design, the magnet strength decays as $1/r^4$ in the far field (r being the radial distance away from the magnet) instead of $1/r^3$, thereby reducing the sensitivity to stray fields. The magnet design has been optimised to generate the required Lorentz force under minimal excitation current. The optimisation process is based on the fundamental equations of electromagnetism and the Biot-Savart law and is extensively described in [42, 43], design details can be found in Appendix. A.

The force-balance operation is applied by closing a lead-lag control loop from the reading of the interferometric sensor to the voice-coil actuator. The open-loop transfer function and open-loop gain are shown in Figure. 5. The control consists of a large proportional gain ($9.76 \cdot 10^6$) combined with a lead action centred at the cross-over frequency of 60 Hz. It also features a DC filter at 10 mHz to prevent DC current injection in the coil, and a low-pass filter at 300 Hz for preventing high-frequency noise injection. The first flexible modes of the mechanics appear at a frequency of 235 Hz and limit the proportional gain to be increased further.

The sensor frequency response has been obtained by comparing the sensor's output acceleration with a reference instrument placed side-by-side. The reference instrument is a Guralp 6T broadband force-feedback seismometer spanning the 30 s - 100 Hz bandwidth. The results are shown in Figure 6. The response of the optical accelerometer with the control loop disabled (corresponding to the ”Passive” trace in Figure. 6) is shown as a reference. It can be seen that the sensor in the FBA configuration successfully demonstrates a broadband response from DC to 60 Hz. The corner frequency of the sensitivity function corresponds to the control unity gain frequency and is limited by the flexible modes of the sensor mechanics. The two sensors show great coherence in the 1 Hz to 100 Hz bandwidth. The coherence drop above 100 Hz correlates to the upper corner frequency of the Guralp instrument, and the sub-1 Hz frequencies of the optical sensor are polluted by control noise, as it will be shown in Figure. 7.

A noise budget of the sensor in the FBA configuration is shown in Figure. 7. The plot shows a spectrum of the sensor's acceleration output (ground), onto which each noise source of the sensors has been superimposed. The Guralp 6-T self-noise and acceleration spectrum are also superimposed for reference. These mostly consist of: the interferometer noise as presented in section III (IFO), the ADC and DAC noises of the data acquisition system (dSapce Microlab box 16-bit real time target), the actuator coil-driver electrical noise, and a model of the sensors thermal noise estimated from the fluctuation-Dissipation theorem [51]. Each of these noise sources, except for thermal noise, are measured individually and are referred to the sensor output following the sensor block diagram shown in Figure. 8. Figure. 7 shows that the sensor achieves a 1 µm/s^2 resolution in the [1 - 100] Hz bandwidth. The sensor resolution is limited over the full bandwidth by DAC and coil driver noise propagating through the control loop. Below 1 Hz, the noise degrades with $f^{-0.5}$ due to electrical Flicker noise and as f^2 due to the interferometer detection noise scaled with the sensor's mechanical response.

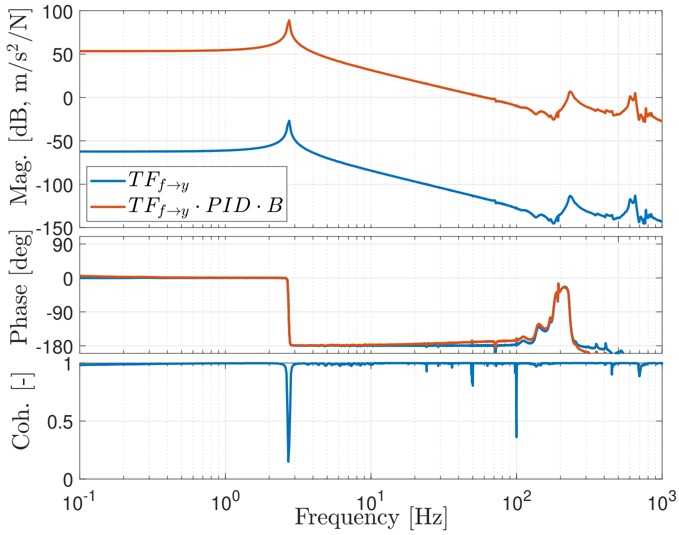

Figure 5: Open-loop transfer functions. It identifies the sensor mechanical resonance at 2.8 Hz with a Q-factor of approximately 200. It shows that the mechanics is clear of spurious modes up to 200 Hz. The open-loop gain is tuned with a cross-over frequency of 60 Hz with a phase margin of 15^o.

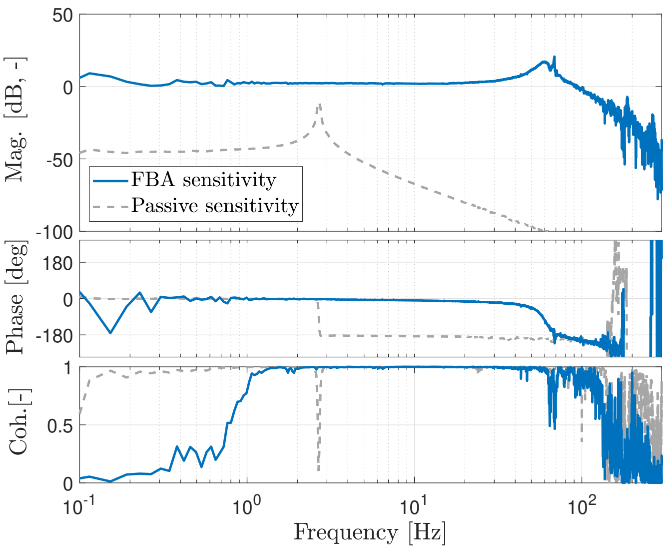

Figure 6: Sensitivity of the sensor with FBA. The sensor in a passive configuration is shown as a reference. The sensitivity is extended flat up to 30 Hz. Flexible modes in the mechanics prevent increasing the control further. The coherence drop below 1 Hz is caused by control noise injection.

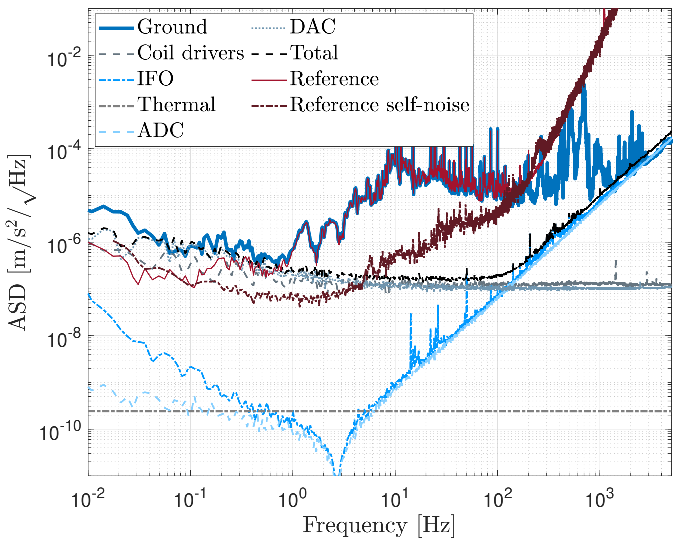

Figure 7: Noise budget of the sensor in the FBA configuration. Ground is the spectrum of accelerometer output placed on solid ground. The trace of an additional sensor (Guralp 6T) is shown for reference together with its self-noise.

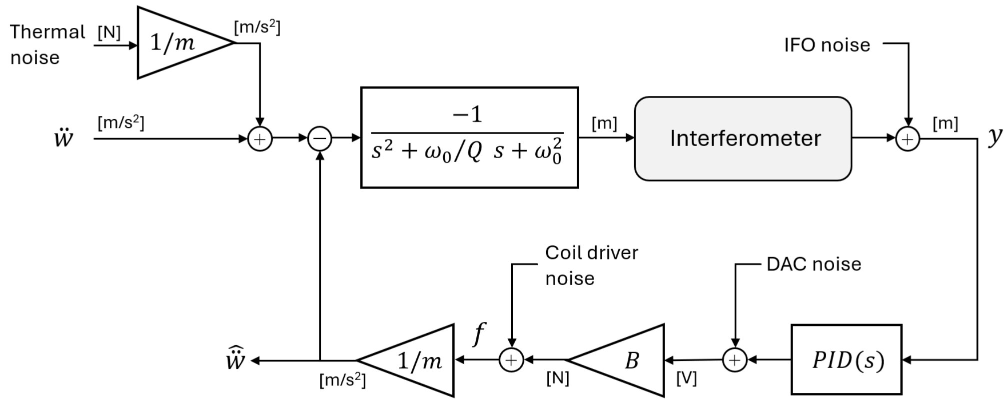

Figure 8: Noise diagram of the optical accelerometer in the FBA configuration. $\ddot{w}$ shows the input acceleration and $\hat{\ddot{w}}$ the measured acceleration. The thermal noise directly couples to the mechanics of the sensor. The interferometer block contains the interferometer noise diagram exposed before, and IFO noise embeds all noise attached to the readout, in particular the ADC noise. $PID(s)$ is the controller of the feedback action loop, B embeds the voice-coil transducer constant [N/A] and the coil driver constant [A/V].

IV.ii Frequency compensation

In the frequency compensation configuration, the sensor feedback loop is left disabled and the response is electronically extended with an appropriate filter. The filter is basically based on the inversion of the sensor's response and replaces it with an "arbitrary" broadband response. Low-pass and high-pass filters are also added to prevent unbounded amplification at low/high frequencies and guarantee the stability of the inversion process. Figure. 10 shows the sensor frequency response obtained with the same reference seismometer placed side-by-side. The stretched response extends from DC to 100 Hz. The inversion process successfully compensates for the sensor's mechanical resonance, and this operation is made robust by adding a thin layer of viscous material underneath the pendulum. The two sensors show great coherence. The coherence drops below 100 mHz and above 100 Hz are the limitations of the Guralp 6T instrument.

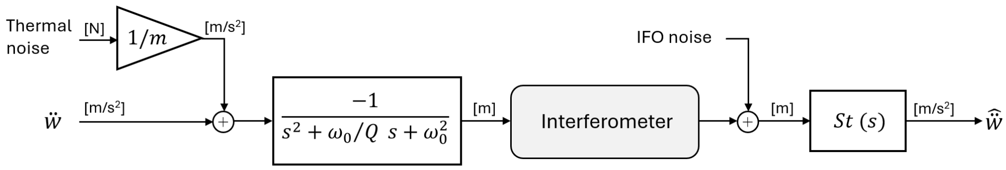

Figure 9: Noise diagram of the optical accelerometer in the stretcher configuration. $\ddot{w}$ shows the input acceleration and $\hat{\ddot{w}}$ the measured acceleration. The thermal noise directly couples to the mechanics of the sensor. The interferometer block contains the interferometer noise diagram exposed before, and IFO noise embeds all noise attached to the readout, in particular the ADC noise. $St(s)$ symbolises the compensation filter.

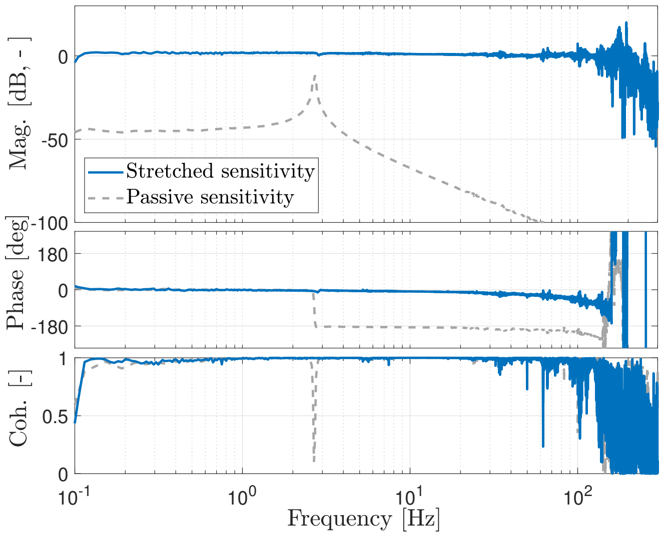

Figure 10: Sensitivity of the sensor in the frequency compensation configuration. The sensor in a passive configuration is shown as a reference. The sensitivity is extended flat up to 100 Hz.

The noise budget of the sensor in the stretched configuration is shown in Figure. 11. The plot shows a spectrum of the sensor's acceleration output (ground), onto which each noise source of the sensors has been superimposed. These mostly consist of: the interferometer noise as presented in section III (IFO noise), the ADC noise of the data acquisition system (dSapce Microlab box 16-bit real time target), and a model of the sensors thermal noise computed using the fluctuation-Dissipation theorem [51]. The reference sensor self-noise and acceleration spectrum are also superimposed for reference. The noises are referred to the sensor output following the sensor block diagram shown in Figure. 9. Figure. 11 shows that the sensor reaches peak performance at 2.8 Hz of 0.3 nm/s^2 limited by mechanical thermal noise. Since there are no control electronics involved, the sensor is solely limited by readout noise which scales as f^2 above the resonance frequency because of the sensor mechanical response, and f^{-1} below the resonance frequency because of assumed thermal effect in the readout. This approach however suffers from optical/mechanical non-linearities since the proof mass is left free to move.

V Conclusion

This paper compared two techniques for extending the frequency bandwidth of a high resolution (long period) accelerometer equipped with a quadrature Michelson interferometric readout. The quadrature Michelson interferometer used as a relative displacement readout demonstrated a resolution below 0.2 pm/$\sqrt{\text{Hz}}$ above a few Hz. The sensitivity is limited by the 16-bit data acquisition system. Two methods are pre-

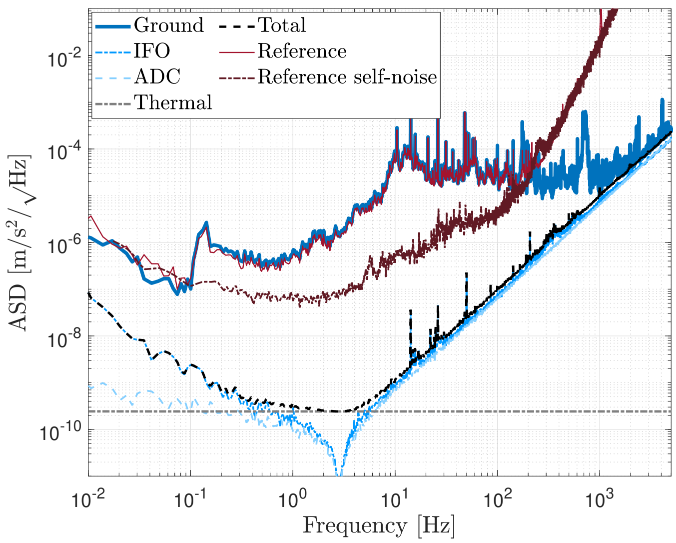

Figure 11: Noise budget of the sensor in the frequency compensation configuration. Ground is the accelerometer output placed on solid ground. The trace of an additional sensor (Guralp 6T) is shown for reference together with its self-noise.

sented and compared for extending the sensor frequency response above the sensor mechanical resonance frequency: the industry-standard force-balance principle and a frequency compensation technique based on an electrical inversion. The measurement of the sensor response in comparison with a reference seismometer shows that both methods can extend the bandwidth to frequencies larger than the resonance frequency of the passive sensor. The FBA is limited to a corner frequency of 60 Hz due to spurious mechanical modes in the controller design. A corner frequency of 100 Hz is achieved for the frequency compensation configuration and is chosen as a trade-off between large bandwidth and high-frequency noise amplification. Resolution-wise, the sensor extended using the force-balance principle is shown to reach a resolution of 1 µm/s^2 in the [1 - 100] Hz bandwidth, limited by control noise injection. This can be improved with a better coil-driver design and lower noise electronics. The frequency compensation configuration is solely limited by the readout noise scaled with the sensor mechanical response and reaches peak performance at 2.8 Hz of 0.3 nm/s^2. While the frequency compensation configuration is control-noise-free, it however suffers from the non-linear behaviour of the interferometer and of the mechanics. This is partially alleviated with a linearisation process prior to demodulating the photodiode signals. Figure. 12 shows a qualitative comparison of the two methods. The noise floors found in this plot are the quadratic sum of the different noises exposed in the previous sections. The upper limit for the dynamic range is set by the range of the control electronics for the optical sensor in the FBA configuration and by the non-linear response of the interferometer for the stretched (open-loop) sensor. Noise floors of various standard low-noise seismometers and accelerometers are also superimposed in the Figure. The numbers are derived from an experimental study from the LIGO Scientific Community (public DCC document number LIGO-T0900450-v5, B. Lantz). The optical accelerometer shows a competing resolution above 1 Hz; the excess noise in the interferometric readout causes the resolution to degrade below 1 Hz compared to STS-2 and T240 instruments. Such a sensor with a broadband response but yet the noise level of a long-period sensor can find application in vibration isolation systems of large-scale, high-end instruments. Namely in gravitational wave detectors and quantum gravimeters whose performance is limited in the [10 mHz - 100 Hz] bandwidth by seismic noise.

Future improvement will report on the development of a low-noise electronic system to reduce control noise in the FBA sensor and therefore benefit from both the high resolution of the optical readout and the linearity of the actuator. The major contributor to control noise is indeed the DAC noise of the 16-bit real-time target system, whose main purpose is to run the ellipse linearisation in real time since this operation is complex to implement in an analogue system. However, the locking of the interferometer with FBA loop raises the question of whether the ellipse fitting algorithm is still required for linearity or not. In the latter case, a large reduction in control noise could be achieved with low-noise analogue control electronics. The stability of the laser source and thermal sensitivity of the system (both mechanical and optical) are also under investigation for improving the excess of low-frequency (below 1 Hz) noise in the interferometric readout.

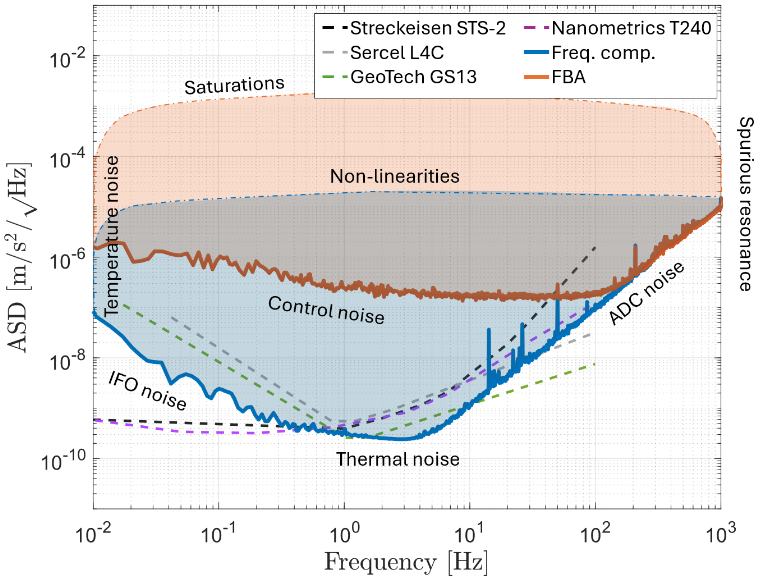

Figure 12: Qualitative comparison of the sensitivity of the two approaches for extending the bandwidth of an inertial accelerometer. The numbers shown here are orders of magnitude representative of the results obtained in this paper. It shows that the frequency compensation method is successful at extending the frequency bandwidth without degrading the performance of the passive sensor, but non-linearities limit dynamic range. The FBA method increases the dynamic range up to the saturation limit of the actuator. However, control noise injection degrades the resolution and spurious mechanical modes limit the frequency range. As a comparison, the noise floors of different standard instruments have been added (LIGO-T0900450-v5).

Acknowledgments

The authors gratefully acknowledge the European Research Council (Consolidator grant ”SILENT” grant agreement number 866259), the Fonds de la Recherche Scientifique (research project grant ”INFuSE” grant agreement number FNRS PDR T.0049.20), and the European Commission (Horizon Europe project ”FIQUgS” grant agreement number 101080144) for funding this research. The authors also acknowledge the LIGO scientific community for reviewing this research. This paper has been assigned the LIGO DCC number P2400535.

References

[1] E. H. Anderson, R. M. Glaese, and D. Neill, “A comparison of vibration damping methods for ground based telescopes,” in *Ground-based and Airborne Telescopes II*, L. M. Stepp and R. Gilmozzi, Eds., vol. 7012, International Society for Optics and Photonics. SPIE, 2008, p. 70120H. [Online]. Available: https://doi.org/10.1117/12.790195

[2] C. Collette, K. Artoos, A. Kuzmin, S. Janssens, M. Sylte, M. Guinchard, and C. Hauviller, “Active quadrupole stabilization for future linear particle colliders,” *Nuclear Instruments and Methods in Physics Research Section A: Accelerators, Spectrometers, Detectors and Associated Equipment*, vol. 621, no. 1, pp. 71–78, 2010. [Online]. Available: https://www.sciencedirect.com/science/article/pii/S0168900210011174

[3] D. DeBra, “Vibration isolation of precision machine tools and instruments,” *CIRP Annals*, vol. 41, no. 2, pp. 711–718, 1992. [Online]. Available: https://www.sciencedirect.com/science/article/pii/S0007850607632570

[4] T. Accadia *et al.*, “The Seismic Superattenuators of the Virgo Gravitational Waves Interferometer,” *Journal of Low Frequency Noise, Vibration and Active Control*, vol. 30, no. 1, pp. 63–79, mar 2011.

[5] T. Akutsu *et al.*, “Vibration isolation systems for the beam splitter and signal recycling mirrors of the KAGRA gravitational wave detector,” *Classical and Quantum Gravity*, vol. 38, no. 6, p. 065011, mar 2021.

[6] R. Abbott, R. Adhikari, G. Allen, D. Baglino, C. Campbell, D. Coyne, E. Daw, D. DeBra, J. Faludi, P. Fritschel, A. Ganguli, J. Giaime, M. Hammond, C. Hardham, G. Harry, W. Hua, L. Jones, J. Kern, B. Lantz, K. Lilienkamp, K. Mailand, K. Mason, R. Mittleman, S. Nayfeh, D. Ottaway, J. Phinney, W. Rankin, N. Robertson, R. Scheffler, D. H. Shoemaker, S. Wen, M. Zucker, and L. Zuo, “Seismic isolation enhancements for initial and advanced LIGO,” *Classical and Quantum Gravity*, vol. 21, no. 5, pp. S915–S921, feb 2004.

[7] J. L. Gouët, T. E. Mehlstäubler, J. Kim, S. Merlet, A. Clairon, A. Landragin, and F. P. D. Santos, “Limits to the sensitivity of a low noise compact atomic gravimeter,” *Applied Physics B*, vol. 92, no. 2, pp. 133–144, jun 2008.

[8] M.-K. Zhou, Z.-K. Hu, X.-C. Duan, B.-L. Sun, L.-L. Chen, Q.-Z. Zhang, and J. Luo, “Performance of a cold-atom gravimeter with an active vibration isolator,” *Physical Review A*, vol. 86, no. 4, oct 2012.

[9] J. Lautier, L. Volodimer, T. Hardin, S. Merlet, M. Lours, F. P. D. Santos, and A. Landragin, “Hybridizing matter-wave and classical accelerometers,” *Applied Physics Letters*, vol. 105, no. 14, p. 144102, oct 2014.

[10] V. Ménoret, P. Vermeulen, N. L. Moigne, S. Bonvalot, P. Bouyer, A. Landragin, and B. Desruelle, “Gravity measurements below 10-9 g with a transportable absolute quantum gravimeter,” *Scientific Reports*, vol. 8, no. 1, aug 2018.

[11] J. M. Hensley, A. Peters, and S. Chu, “Active low frequency vertical vibration isolation,” *Review of Scientific Instruments*, vol. 70, no. 6, pp. 2735–2741, 06 1999. [Online]. Available: https://doi.org/10.1063/1.1149838

[12] V. Greco, G. Molesini, and F. Quercioli, “Accurate polarization interferometer,” *Review of Scientific Instruments*, vol. 66, no. 7, pp. 3729–3734, jul 1995.

[13] J. Watchi, S. Cooper, B. Ding, C. M. Mow-Lowry, and C. Collette, “Contributed Review: A review of compact interferometers,” *Review of Scientific Instruments*, vol. 89, no. 12, p. 121501, dec 2018.

[14] S. J. Cooper, C. J. Collins, A. C. Green, D. Hoyland, C. C. Speake, A. Freise, and C. M. Mow-Lowry, “A compact, large-range interferometer for precision measurement and inertial sensing,” *Classical and Quantum Gravity*, vol. 35, no. 9, p. 095007, mar 2018.

[15] J. Smetana, R. Walters, S. Bauchinger, A. S. Ubhi, S. Cooper, D. Hoyland, R. Abbott, C. Baune, P. Fritchel, O. Gerberding, S. Köhnke, H. Miao, S. Rode, and D. Martynov, “Compact michelson interferometers with subpicometer sensitivity,” Feb. 2022.

[16] A. J. Sutton, O. Gerberding, G. Heinzel, and D. A. Shaddock, “Digitally enhanced homodyne interferometry,” *Optics Express*, vol. 20, no. 20, p. 22195, sep 2012.

[17] C. Sternkopf, C. Diethold, U. Gerhardt, J. Wurmus, and E. Manske, “Heterodyne interferometer laser source with a pair of two phase locked loop coupled he–ne lasers by 632.8 nm,” *Measurement Science and Technology*, vol. 23, no. 7, p. 074006, jun 2012.

[18] J. D. Otero, "Development and Characterization of an Observatory-class,Broadband, Non-Fedback, Leaf-Spring Interferometric Seismometer," Ph.D. dissertation, University of California, 2009.

[19] M. Zumberge, J. Berger, J. Otero, and E. Wielandt, "An optical seismometer without force feedback," *Bulletin of the Seismological Society of America*, vol. 100, no. 2, pp. 598–605, mar 2010.

[20] M. Zumberge, J. Berger, W. Hatfield, and E. Wielandt, "A three-component borehole optical seismic and geodetic sensor," *Bulletin of the Seismological Society of America*, vol. 108, no. 4, pp. 2022–2031, May 2018.

[21] J. Berger, P. Davis, R. Widmer-Schnidrig, and M. Zumberge, "Performance of an optical seismometer from 1 hz to 10 hz," *Bulletin of the Seismological Society of America*, vol. 104, no. 5, pp. 2422–2429, Aug. 2014.

[22] S. J. Cooper, C. J. Collins, L. Prokhorov, J. Warner, D. Hoyland, and C. M. Mow-Lowry, "Interferometric sensing of a commercial geophone," *Classical and Quantum Gravity*, vol. 39, no. 7, p. 075023, mar 2022.

[23] J. V. van Heijningen, A. Bertolini, and J. F. J. van den Brand, "A novel interferometrically read out inertial sensor for future gravitational wave detectors," in *2018 IEEE Sensors Applications Symposium (SAS)*. IEEE, mar 2018.

[24] C. Collette, F. Nassif, J. Amar, C. Depouhon, and S.-P. Gorza, "Prototype of interferometric absolute motion sensor," *Sensors and Actuators A: Physical*, vol. 224, pp. 72–77, apr 2015.

[25] B. Ding, G. Zhao, J. Watchi, A. Sider, and C. Collette, "An interferometric inertial sensor for low-frequency seismic isolation," *Sensors and Actuators A: Physical*, vol. 335, p. 113398, mar 2022.

[26] F. C. Guzman, L. Kumanchik, J. Pratt, and J. Taylor, "High sensitivity optomechanical reference accelerometer over 10 kHz."

[27] E. Davies, D. S. George, M. C. Gower, and A. S. Holmes, "Optical accelerometer with mechanical amplification via a V-beam mechanism," in *2013 IEEE 26th International Conference on Micro Electro Mechanical Systems (MEMS)*. IEEE, jan 2013.

[28] A. Hines, L. Richardson, H. Wisniewski, and F. Guzman, "Optomechanical Inertial Sensors," *Appl. Opt.*, 2020.

[29] C. Collette, S. Janssens, P. Fernandez-Carmona, K. Artoos, M. Guinchard, C. Hauviller, and A. Preumont, "Review: Inertial Sensors for Low-Frequency Seismic Vibration Measurement," *Bulletin of the Seismological Society of America*, vol. 102, no. 4, pp. 1289–1300, aug 2012.

[30] M. J. Usher, R. F. Burch, and C. Guralp, "Wide-band feedback seismometers," *Physics of the Earth and Planetary Interiors*, vol. 18, no. 2, pp. 38–50, feb 1979.

[31] A. Plešinger and J. Buben, "Analysis and optimization of wide-band force-balance seismometer responses," *Studia Geophysica et Geodaetica*, vol. 28, no. 1, pp. 67–81, mar 1984.

[32] M. A. Riedesel, J. A. Orcutt, and R. D. Moore, "Limits of sensitivity of inertial seismometers with velocity transducers and electronic amplifiers," *Bulletin of the Seismological Society of America*, vol. 80, no. 6A, pp. 1725–1752, Dec. 1990.

[33] J. Smetana, C. Di Fronzo, A. Amorosi, and D. Martynov, "Nonlinearities in fringe-counting compact michelson interferometers," *Sensors*, vol. 23, no. 17, 2023. [Online]. Available: https://www.mdpi.com/1424-8220/23/17/7526

[34] A. Garimella and P. M. Furth, "Frequency compensation techniques for op-amps and ldos: A tutorial overview," in *2011 IEEE 54th International Midwest Symposium on Circuits and Systems (MWSCAS)*. IEEE, Aug. 2011, pp. 1–4.

[35] B. Ding, G. Zhao, J. Watchi, and C. Collette, "Huddle test of optical inertial sensors combined with slightly damped mechanics," 2018.

[36] B. Ding, "Development of High Resolution Interferometric Inertial Sensors ," Ph.D. dissertation, Université Libre de Bruxelles, 2021.

[37] J. Watchi, B. Ding, F. Matichard, and C. Collette, "Development of a high-resolution optical inertial sensor for sub-hz seismic isolation," *Proceedings of ISMA including USD*, 09 2016.

[38] J. Watchi, "Active seismic isolation using interferometric inertial sensors," Ph.D. dissertation, Université Libre de Bruxelles, 2022.

[39] M. A. Zumberge, J. Berger, M. A. Dzieciuch, and R. L. Parker, "Resolving quadrature fringes in real time," *Applied Optics*, vol. 43, no. 4, p. 771, Feb. 2004.

[40] E. Wielandt and G. Streckeisen, "The leaf-spring seismometer: Design and performance," *Bulletin of the Seismological Society of America*, vol. 72, no. 6A, pp. 2349–2367, dec 1982.

[41] L. J. B. LaCoste, "A new type long period vertical seismograph," *Physics*, vol. 5, no. 7, pp. 178–180, jul 1934.

[42] G. Fortman, "Instruments for seismici solation," Ph.D. dissertation, Delft University of Technology, 2019.

[43] A. Mitchell, "Coil drivers with shielding magnets in the 6d inertial isolation system," *LIGO Document T2100132*, 2021.

[44] A. Mitchell, A. Ubhi, C. Mow-Lowry, and L. Prokhorov, "Coil drivers with shielding magnets in the 6d inertial isolation system," *LVK conference poster*, 2021.

[45] N. Robertson, "Beamsplitter actuation: Potential use of shielding magnets." *LIGO Document T1500535*, 2019.

[46] A. Amorosi, L. Amez-Droz, M. Teloi, M. H. Lakkis, B. Ding, J. Watchi, C. Di Fronzo, R. Jamshidi, P. Lambert, and C. Collette, "High resolution compact vertical inertial sensor for atomic quantum gravimeter hybridization," *ISMA-USD Noise and Vibration Engineering Conference 2022*, 01 June 2022.

[47] P. J. Esrom, "Sensors and signal conditioning, by r. pallas-areny and j.g. webster j. wiley and sons, new york and chichester (uk), 1991 xii 398pp., index (£47.50)." *Robotica*, vol. 10, no. 5, p. 472–472, 1992.

[48] T. van der Poel, "An exploration of active hard mount vibration isolation for precision equipment," Ph.D. dissertation, 2010.

[49] J. B. Johnson, "Thermal agitation of electricity in conductors," *Phys. Rev.*, vol. 32, pp. 97–109, Jul 1928. [Online]. Available: https://link.aps.org/doi/10.1103/PhysRev.32.97

[50] T. Kuparowitz, "Assessment of Noise Sources in Resistors," 2015.

[51] P. R. Saulson, "Thermal noise in mechanical experiments," *Physical Review D*, vol. 42, no. 8, pp. 2437–2445, oct 1990.

Appendix

A Quadrupole voice-coil design

The quadrupole magnet design and optimisation process is based on solving the equations of electromagnetism and Biot-Savart law for a quadrupole magnet. The equations of the magnetic field of a quadrupole magnetic field have been derived in [42]. The force output of such a coil and magnet configuration depends on the coil and magnet characteristics. In this paper, the actuator uses the coil of a moticont lvcm-022-013-02 voice-coil motor. Relevant parameters can be found in the product datasheet. The parameters of the quadrupole magnet have been optimised to maximize the actuator constant with a design that fits the coil while allowing an acceptable radial clearance of at least 1 mm to tolerate the angular motion of the magnet. The relevant parameters are the size of the magnets, the distance of the magnet assembly to the coil centre, and the inter-magnet distance. Figure 13 shows a schematic drawing of the custom quadrature magnet design. N45 Neodymium disc magnets are used for their large magnetic strength. The magnets are 12 mm in diameter and 3 mm thick to fit the mechanics with an acceptable clearance. A 5 mm inter-magnet distance has been optimised to allow a good far-field cancellation of the magnetic flux lines while still allowing an acceptable force per unit current to be generated by the coil. All parameters can be found in Table. 1.

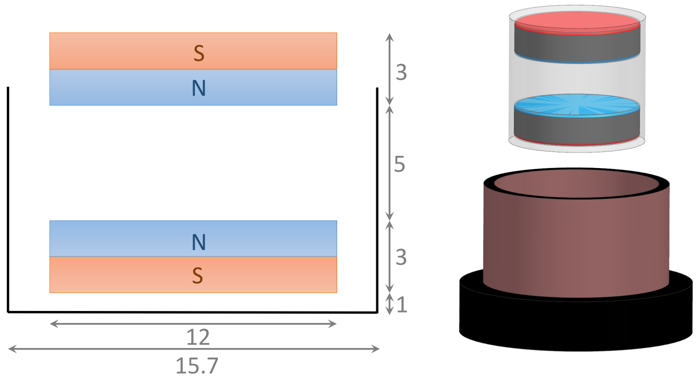

Figure 13: Schematic drawing of the double magnet voice-coil (left) and CAD view (right). The Neodymium magnets are shown as the blue/orange blocks, the coil is drawn in black and characteristic dimensions are shown in grey. The double magnet assembly is embedded in a casing made of a non-magnetic material.

Table 1: Quadrupole voice-coil actuator design parameters.

Coil parameters		Magnet parameters	
Inner diameter [mm]	15.7	Material	N45 Neodymium
Height [mm]	9.5	Distance to coil centre [mm]	2.5
Number of turns [-]	165	Magnet diameter [mm]	12
Wire material [-]	Copper	Magnet height [mm]	3
Coil inductance [Ω]	4.9	Inter-magnet distance [mm]	5

The numerical model in Python of the voice-coil force constant using the Biot-Savart equations is depicted in Figure 14 (left). It shows a force constant of 0.59 N/A. Finite element modelling using the FEEM 4.2 software further validated this model. The voice-coil has been produced and experimentally characterised in Figure 14(right). The force constant has been measured by mounting the voice coil on a scale, and measuring the pulling/pushing force of the actuator when injecting constant current into the coil. The weight reading of the scale can be up-converted to a force by multiplying the mass reading by the gravitational acceleration, with a reading accuracy of 0.01 g. The voice coil demonstrated a force constant of 0.6465 N/A, and good linearity even under input currents up to 600 mA. Assuming an RMS value for the ground motion of typically a few micrometres, it can be computed from the pendulum mechanical properties ($m = 0.4$ kg, $f_0 = 2.8Hz$) and location of the force actuator (35 mm lever-arm distance from the joint) that a peak force of 5 mN would be required to balance the pendulum motion under normal seismic conditions. This leads to an average actuation current of 8.5 mA.

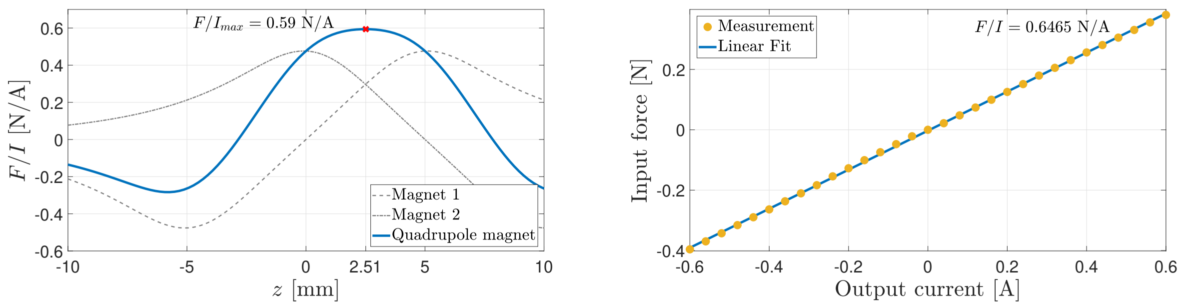

Figure 14: (left) Design force per unit current of the custom voice-coil. z represents the distance of the magnet assembly to the coil centre. The Lorentz forces applied on each individual magnet are shown as grey lines, and the resulting force is shown in blue. The voice coil has a maximum force constant of 0.6 N/A in the optimal position. (right) Experimental force output of the custom voice-coil actuator. The voice coil was mounted on a scale and fed with DC current. The weight reading on the scale can be converted to a force reading measurement. The force constant of 0.6465 N/A has been measured.